



2022 DRAGON 5 SYMPOSIUM

MID-TERM RESULTS REPORTING

17-21 OCTOBER 2022

PROJECT ID. 154

**GLOBAL CLIMATE CHANGE, SEA LEVEL RISE,
EXTREME EVENTS AND LOCAL GROUND
SUBSIDENCE EFFECTS IN COASTAL AND RIVER
DELTA REGIONS THROUGH NOVEL AND
INTEGRATED REMOTE SENSING APPROACHES
(GREENISH)**



18 OCTOBER 2202

ID. 154

PROJECT TITLE: GREENISH

PRINCIPAL INVESTIGATORS: ANTONIO PEPE, QING ZHAO

CO-AUTHORS: FABIANA CALÒ, PIETRO MASTRO, CARMINE SERIO, GUIDO MASIELLO, FRANCESCO FALABELLA, FUSUN BALIK SANLI, SAYGIN ABDIKAN, JIAMI PAN, ADAM DEVLIN, TIANLIANG YANG, JINXIN LIN, XINLEI, HUANG, YIXIAN TANG, CHAO WANG, KUN TAN, WEN CHEN, JINGJING WANG, PENG CHEN, ZHENGJIE LI, CHENGFANG YAO

PRESENTED BY: ANTONIO PEPE



Project Objectives

- ❖ Coastal zones are essential for the socio-economic well-being of many nations. Coastal regions are the location of large population centres, have multiple uses, needs and opportunities, and are particularly exposed to extreme events and climate change.
- ❖ The combined effects of sea level rise (SLR), tidal evolution, modulated ocean currents and extreme events can have numerous impacts to coastal, river delta, and inland water zones, including water management
- ❖ Global sea-level is rising, and tides are also changing worldwide and these risks are accompanied by increasing concerns about the growing urbanization of the world's low-lying coastal regions and related coastal hazards (e.g., flooding).



Project Objectives

- ❖ The main goal of the project is the well-use of Earth Observation (EO) data and in-situ monitoring information, to detect the long-term evolution of coastal, deltaic and lake-river systems.
- ❖ Some information related to recent publications and research activities will shortly be given in the following.
- ❖ Also, over the last year, we focused on the development and testing of InSAR, Change Detection and AI methods that can widely be applied in broad contexts and specifically in the selected areas (as to be done in the next two years).





Data access (list all missions and issues if any). NB. in the tables please insert cumulative figures (since July 2021) for no. of scenes of high bit rate data (e.g. S1 100 scenes). If data delivery is low bit rate by ftp, insert "ftp"


ESA Third Party Missions	No. Scenes
1. CSK	10
2.	
3.	
4.	
5.	
6.	
Total:	10
Issues:	

ESA, Explorers & Sentinels data	No. Scenes
1.SENTINEL-1A/B	400
2.SENTINEL-2	10
3.	
4.	
5.	
6.	
Total:	410
Issues:	

Chinese EO data	No. Scenes
1.	
2.	
3.	
4.	
5.	
6.	
Total:	
Issues:	





Name	Institution	Poster title	Contribution
<p>Zhengjie Li^{1,2,3}, Qing Zhao^{1,2,3,*}, Jingjing Wang^{1,2,3}, Chengfang Yao^{1,2},</p>	<p>¹Key Laboratory of Geographical Information Science, Ministry of Education, East China Normal University, Shanghai 200062, China; ²School of Geographic Sciences, East China Normal University, Shanghai 200241, China ; ³Key Laboratory of Spatial-Temporal Big Data Analysis and Application of Natural Resources in Megacities, Ministry of Natural Resources, Shanghai 200241, China</p>	<p>Assessment of Natural Disaster mitigation Capability and Crucial Index at District Level in Shanghai with TOPSIS: A Case Study of Xuhui District</p>	
<p>Chengfang Yao^{1,2,3}, Qing Zhao^{1,2,3*}</p>	<p>1 Key Laboratory of Geographical Information Science, East China Normal University, Shanghai, China 2 Chongming ECO Institute, East China Normal University, Shanghai, China 3 School of Geographic Sciences, East China Normal University, Shanghai, China</p>	<p>The Retrieval of recent-decade ground deformation time-series of Chongming Island in Shanghai with multi-platform MT-InSAR analysis</p>	
<p>Chen Peng^{1,2,3}, Qing Zhao^{1,2,3}, Maochuan Tang^{1,2,3}</p>	<p>1Key Laboratory of Geographical Information Science, Ministry of Education, East China Normal University, Shanghai 200241, China; 2School of Geographic Sciences, East China Normal University, Shanghai 200241, China; 3Key Laboratory of Spatial-Temporal Big Data Analysis and Application of Natural Resources in Megacities, Ministry of Natural Resources, Shanghai 200241, China</p>	<p>A Novel Change Detection Method of Urban Area Based on Res-UNet with Coherence and Intensity Characteristics of SAR Time-Series Images</p>	
			



Name	Institution	Poster title	Contribution
Pietro Mastro	University of Basilicata	Coherent/Incoherent Change Detection Experiments using Sentinel-1 SAR Data	<u>Principal Investigator</u> The paper investigates the role of Change Detection and InSAR methods for the Retrieval and Track of Changes in Inunated/Fire-Prone Regions
Francesco Falabella	University of Basilicata – National Research Council of Italy (CNR)	Non-Closure Phase of Multi-look InSAR Triplets: A New Algorithm for the Mitigation of Phase Bias Phenomena	<u>Principal Investigator</u> The paper describes the problem of potential ground velocity biases in the estimates done using SB-oriented multi-temporal InSAR approaches: the impact on Sentinel-1 Deformation Time-Series Generation.





Exchange Activities and Recruitment Plans

- ❑ Chinese students are working remotely with people at the CNR in Italy
- ❑ After COVID-19 epidemic crisis, a new visit to East China Normal University, Shanghai and at the Chinese Academy of Science (CAS) will be planned
- ❑ I have been selected to be part of the Chinese High-End Foreign Experts Recruitment Program that funds periods of exchange in China, seminars, on-line teaching and various other resources.
- ❑ The recruitment of Two Research Grants (Assegno di Ricerca) for Young Scientists (< 35 years old), financed by ESA and co-financed with other CNR internal funds, is currently in progress. YSs will formally be part of CNR from November 1, 2022.





The schedule of the GREENISH YS recruitment and training (Gaant Chart) is pictorially shown in Figure 1

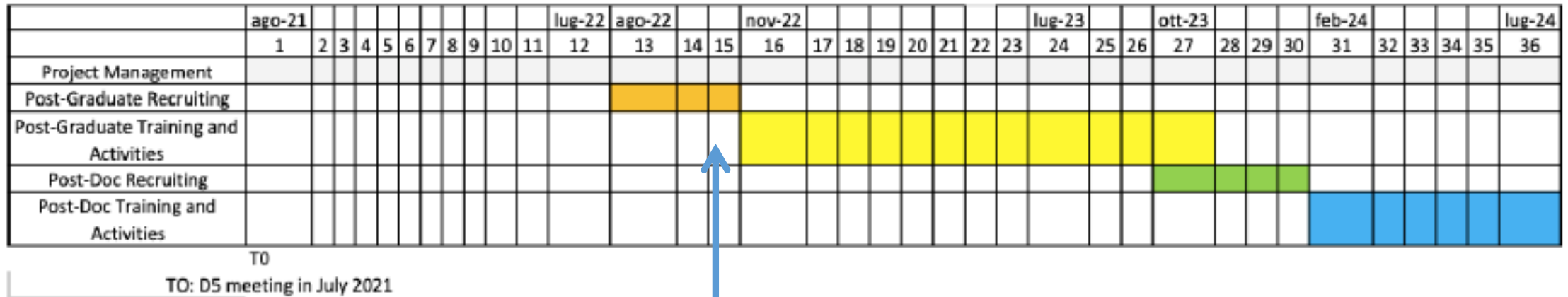





Figure 1: Gaant Chart



*remote sensing**Article*

Changes of Chinese Coastal Regions Induced by Land Reclamation as Revealed through TanDEM-X DEM and InSAR Analyses

Maochuan Tang^{1,2,3}, Qing Zhao^{1,2,3,*}, Antonio Pepe⁴, Adam Thomas Devlin^{5,6,7}, Francesco Falabella^{4,8,9},
Chengfang Yao^{1,2,3} and Zhengjie Li^{1,2,3}

¹ Key Laboratory of Geographical Information Science, Ministry of Education, East China Normal University, Shanghai 200241, China; 51193901043@stu.ecnu.edu.cn (M.T.); 51203901043@stu.ecnu.edu.cn (C.Y.); 51203901076@stu.ecnu.edu.cn (Z.L.)

² Institute of Eco-Chongming (I.E.C.), East China Normal University, Shanghai 202162, China

³ School of Geographic Sciences, East China Normal University, Shanghai 200241, China

⁴ Institute for Electromagnetic Sensing of the Environment (IREA), Italian National Research Council, 328, Diocleziano, 80124 Napoli, Italy; pepe.a@irea.cnr.it (A.P.); francesco.falabella@unibas.it (F.F.)

⁵ Key Laboratory of Poyang Lake Wetland and Watershed Research of Ministry of Education, Nanchang 330022, China; atdevlin@jxnu.edu.cn

⁶ School of Geography and Environment, Jiangxi Normal University, Nanchang 330022, China

⁷ Institute of Space and Earth Information Science, The Chinese University of Hong Kong, Shatin, Hong Kong, China

⁸ Institute of Methodologies for Environmental Analysis (IMAA), Italian National Research Council, Tito Scalo, 85050 Potenza, Italy

⁹ School of Engineering, University of Basilicata, 85100 Potenza, Italy

* Correspondence: qzhao@geo.ecnu.edu.cn; Tel.: +86-21-62224459





- Coastal topography in China has changed significantly over the last two decades due to human actions, such as the development of extensive land reclamation projects. Under climate change effects, potential flood risks in ocean-reclaimed regions are likely to increase including more frequent storm surges and sea level rise.
- However, the effects of potential inundations over new reclamation platforms, which is the coastal zones with low-elevation, have rarely been investigated.
- Furthermore, coastal subsidence can trigger displacements of the seawall crest heights and increase the probability of wave overtopping in the case of an extreme weather event.

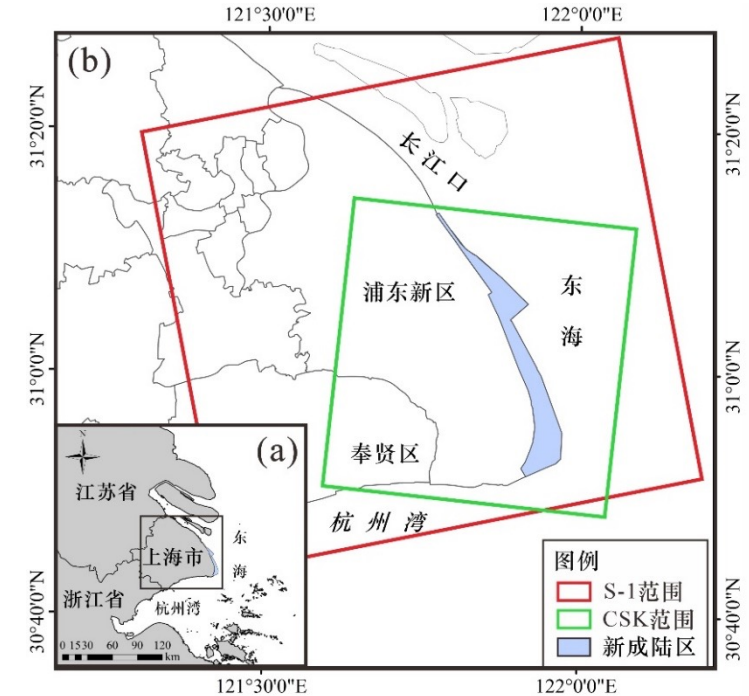


To this purpose, two independent sets of SAR data collected by COSMO-SkyMed (CSK) and Sentinel-1 (S-1) sensors were exploited. We estimated the probability of waves overtopping . Also, we evaluated the impact on the territory of potential extreme flood events.



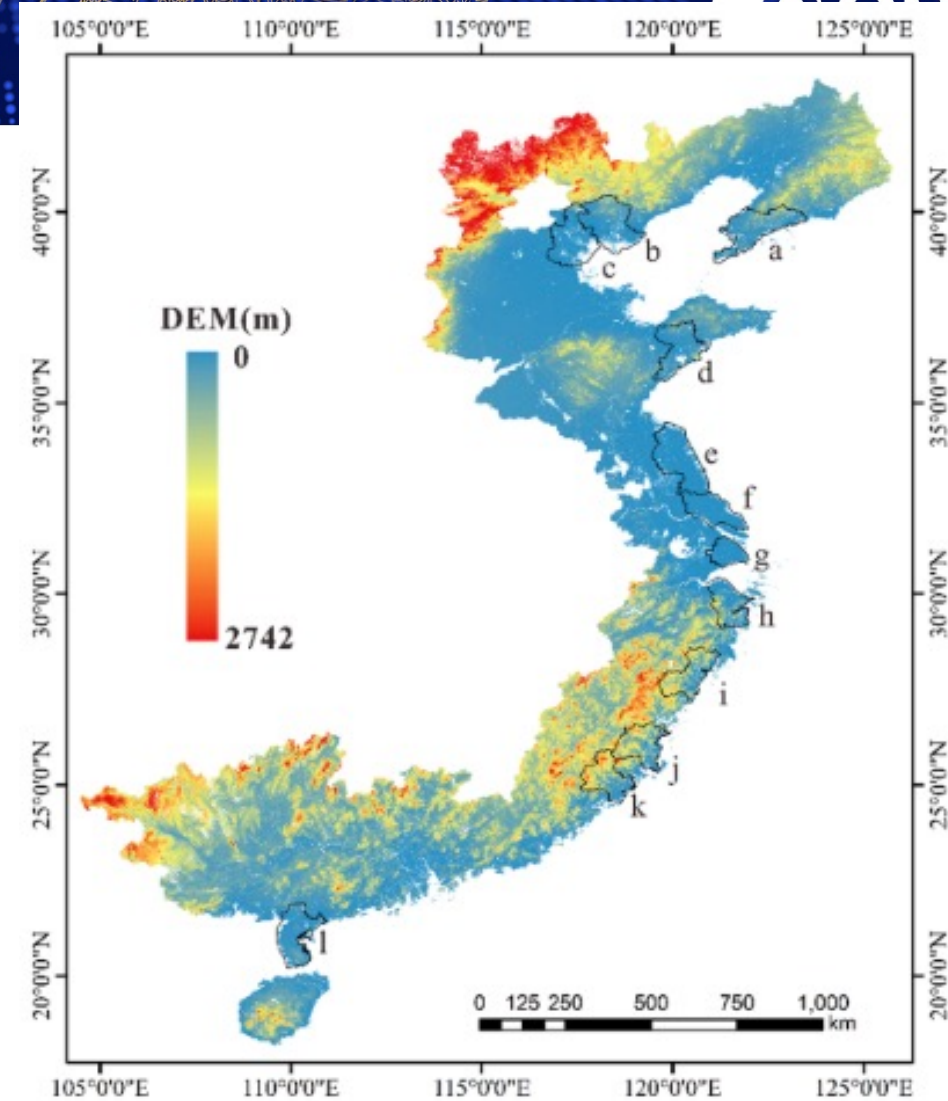
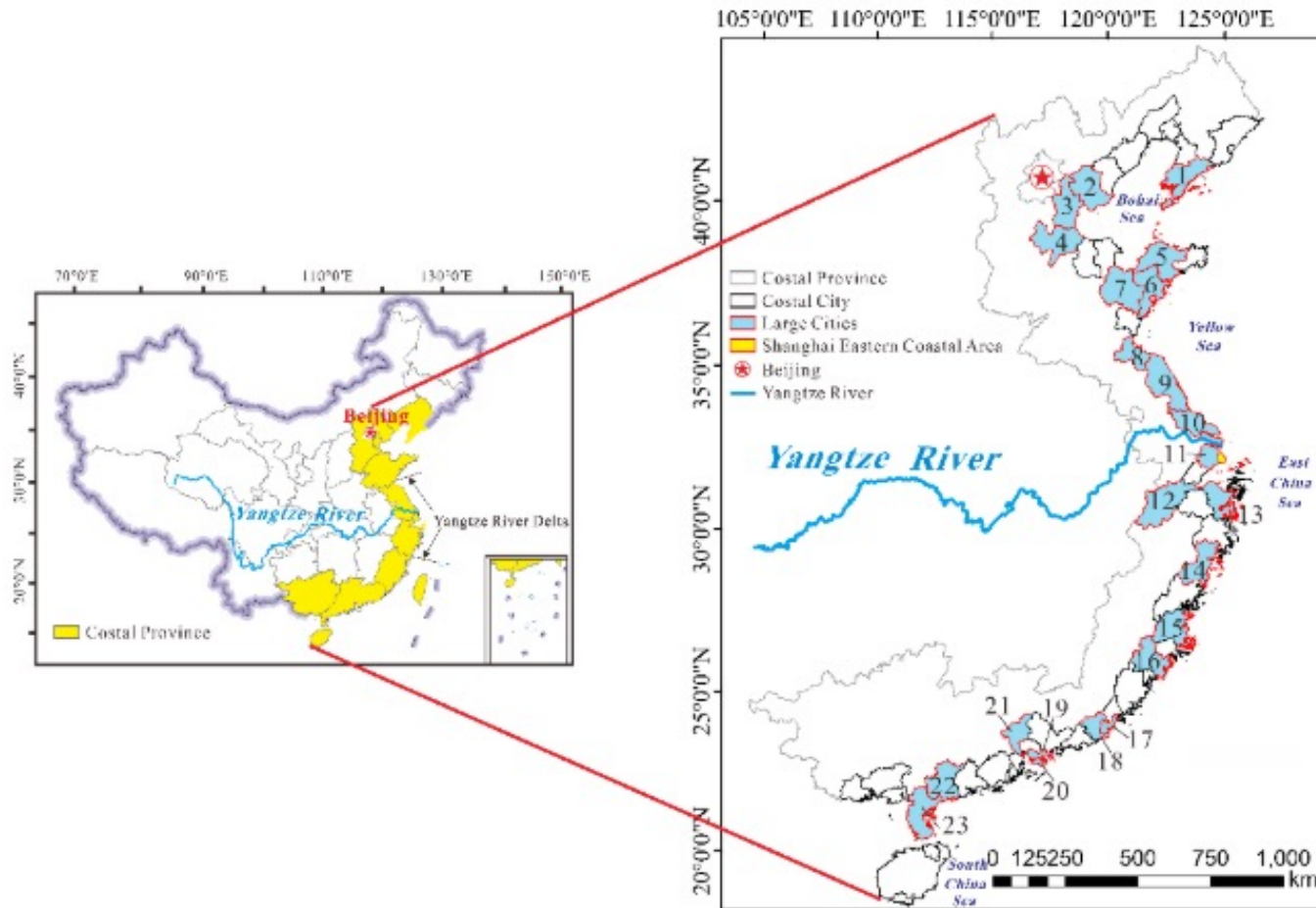


Name	Description
Multi-platform SAR datasets	Ascending Sentinel-1 and descending COSMO-SkyMed images
Seawall height	Obtained in 2010 (Yin, 2020)
GTSR extreme sea levels	1 in 100-year sea levels (Muis, 2016)
TanDEM-X DEM	TDX DEM was acquired during 2010 to 2015. It is relatively new and with 90m spatial resolution.
SRTM DEM	The SRTM DEM was acquired in 2000 The spatial resolution is 30m.
GlobeLand30 land coverage dataset	Spatial resolution is 30 m



The coverages of the Sentinel-1(S-1) and COSMO-SkyMed (CSK) data





The location of the coastal provinces of China and the Yangtze River Delta, and the large cities on the coast of mainland China.

TDX90 DEM of the provinces on the coast of mainland China.





1. Small Baseline Subset (SBAS)

LOS-projected ground deformation time series can be retrieved by using the SBAS method (Berardino, 2002).

$$\Delta\varphi_k(x, r) = \varphi(t_j, x, r) - \varphi(t_i, x, r) \approx \frac{4\pi}{\lambda} [d(t_j, x, r) - d(t_i, x, r)]$$

$$A\varphi = \Delta\varphi$$

$$d(x, r) = \frac{\lambda}{4\pi} \varphi(x, r)$$

λ is the RADAR wavelength ; $d(t_j, x, r)$ and $d(t_i, x, r)$ are the LOS-projected cumulative deformations; A is the M*N coefficient matrix; φ is the phase; $\Delta\varphi$ is a matrix consists of phase difference.

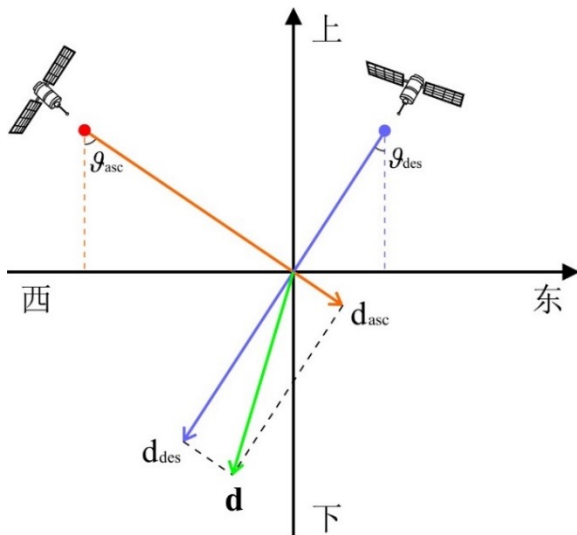




2. Minimum Acceleration Combination (MinA) Method

MinA is a technique for the retrieval of the 3-D Earth's surface deformation time series, through the combination of independently measured LOS displacement time series (Pepe et al., 2016).

S-1 and CSK fly along near-polar orbits (i.e., satellite azimuthal direction is approximately parallel to N-S)



$$\mathbf{d}(P) = \sin \vartheta (P) \cos \varphi(P) \mathbf{e}(P) + \sin \vartheta (P) \sin \varphi(P) \mathbf{n}(P) + \cos \vartheta (P) \mathbf{h}(P)$$

East-West

North-South

Up-Down



$$\mathbf{d}(P) = \sin \vartheta (P) \mathbf{e}(P) + \cos \vartheta (P) \mathbf{h}(P)$$

$$\begin{cases} \lambda (V_{E_{j+1}} - V_{E_j}) = 0 & j = 1, \dots, Q - 2 \\ \lambda (V_{U_{j+1}} - V_{U_j}) = 0 & j = 1, \dots, Q - 2 \end{cases}$$

$$\begin{bmatrix} \mathbf{B} \\ \mathbf{C} \end{bmatrix} \cdot \begin{bmatrix} \mathbf{V}_E \\ \mathbf{V}_U \end{bmatrix} = \begin{bmatrix} \mathbf{d}^{(1)} \\ \mathbf{d}^{(2)} \\ \dots \\ \mathbf{d}^{(N)} \\ 0 \end{bmatrix}$$





3. Seawall Failure Assessment: Probability of Overtopping

We considered that the extreme sea level is not a constant number and could be perturbed higher or lower under the influence of climatic factors (Graff, 1981; Yang, 2015).

Corrected seawall height given by:

$$H(t_2, lon, lat) = H(t_1, lon, lat) + V_{up-down}(t_2 - t_1)$$

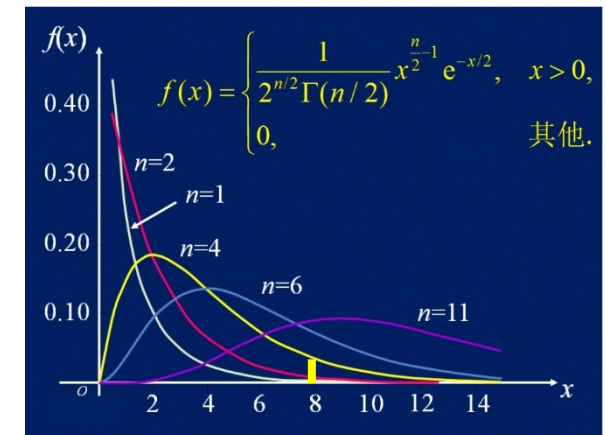
Extreme still water level had a Pearson distribution, and the probability chi-square density function (PDF) is:

$$f(x) = \frac{1}{2^{n/2} \Gamma(n/2)} x^{n/2-1} e^{-x/2}$$

Where n (integer number) is the degree of freedom; x is the water level; and Γ is the gamma function

The probability of overtopping can be calculated as :

$$P(\text{Water-level} \geq \text{Seawall-height}) = 1 - P(\text{Water-level} < \text{Seawall-height})$$



The probability chi-square density function





4、 LISFLOOD-FP Hydrodynamic Model

The model describes the dynamic propagation of wave on floodplain using continuity and momentum equations, discretized over a grid mesh (Bates, 2000; Bates, 2010).

Neglecting the convective acceleration term in the Saint-Venant equation, the momentum equation becomes:

$$\frac{\partial q}{\partial t} + \frac{gh\partial(h+z)}{\partial x} + \frac{gn^2q^2}{R^{\frac{4}{3}}h} = 0$$

Discretizing the equation with respect to time produces:

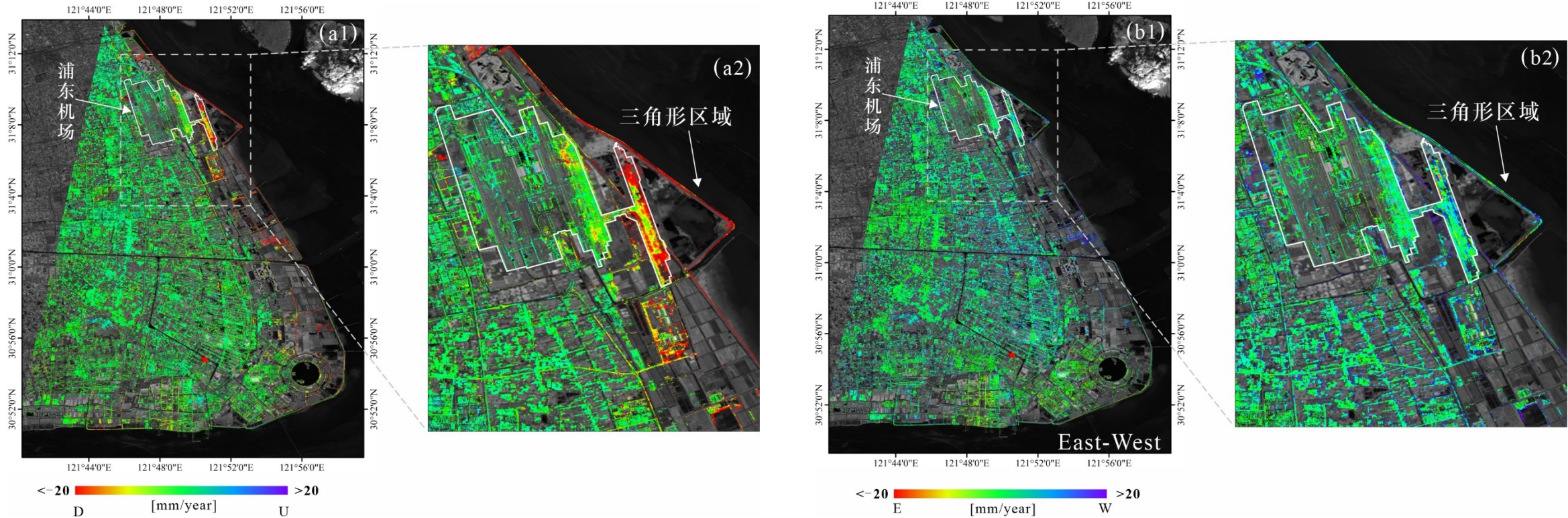
$$q_{t+\Delta t} = \frac{q_t - gh_t\Delta t \frac{\partial(h_t+z)}{\partial x}}{\left(1 + gh_t\Delta tn^2 \frac{q_t}{h_t^{10/3}}\right)}$$

Where q is the flow per unit width, g is the acceleration due to gravity, R is the hydraulic radius, z is the bed elevation, h is the water depth, and n is the Manning's roughness coefficient (0.05).





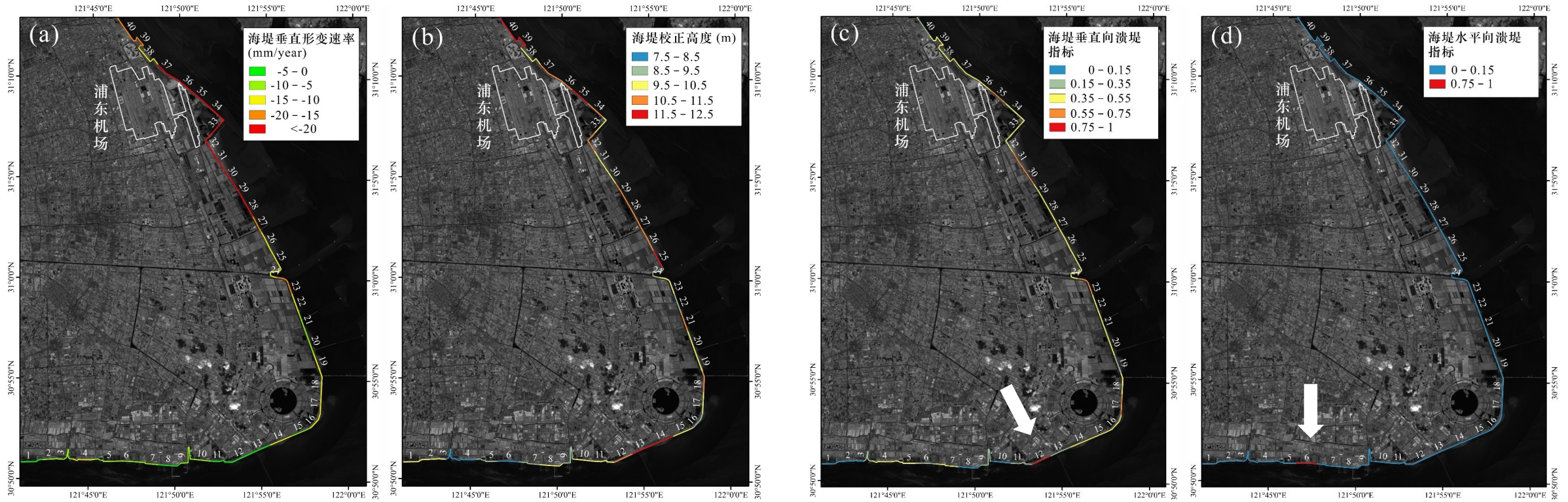
1. 2-D Ground Deformation Results



Maps of Up-Down (a1) and East-West (b1) mean deformation velocity of Shanghai from 2018-2021, and their partial enlarged views (a2) and (b2), respectively.



2. Information Retrieved from the Analysis of 2-D Ground Deformation Results



(a) Deformation velocity map of 40 segments, which obtained from vertical deformation filed of Shanghai. (b) Map of corrected seawall heights of 40 segments considering ground subsidence.

Maps of vertical (a) and horizontal (b) deformation fluctuations for 40 segments in Shanghai.





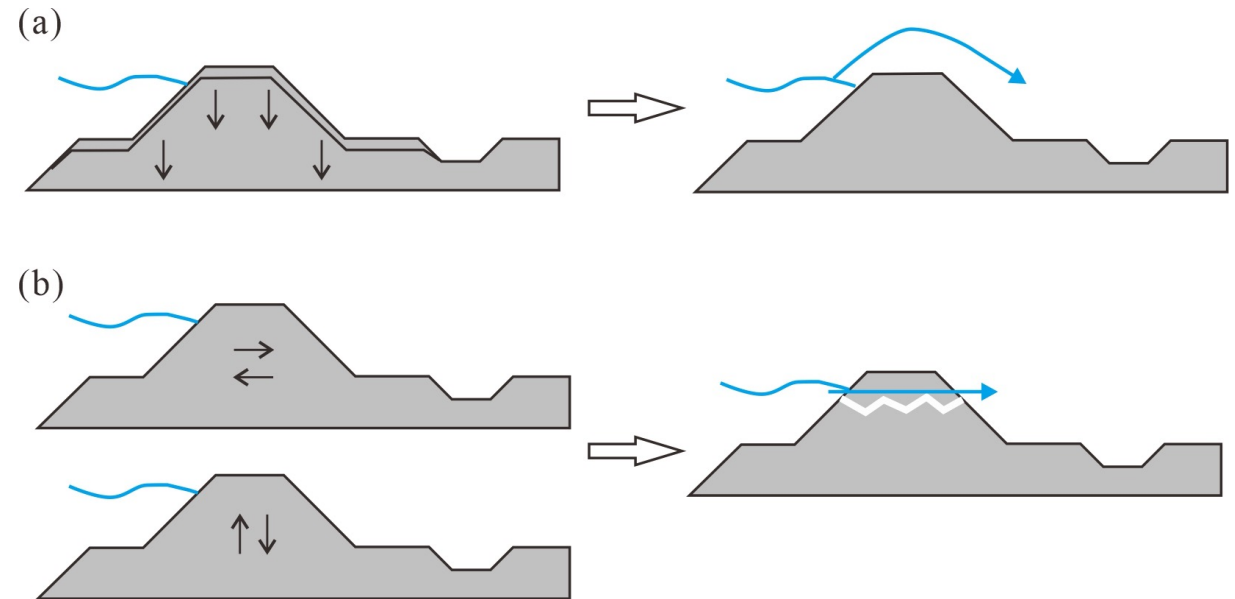
➤ Failure Modes of Seawall

Overtopping

- Mechanism: The water level in front of the dike exceeds the height of the dike.
- Reasons: The dike becomes lower due to subsidence, long-term sea-level rise, extreme sea-level due to storm surges

Levee-breach

- Mechanism: Uneven deformation in the horizontal or vertical directions of seawalls
- Reasons: Ship colliding, waves crashing, pressure of the high water levels, soil characteristics, man-made influence



Sketch map of two failure modes of seawall, including wave overtopping (a) and levee-breach (b).





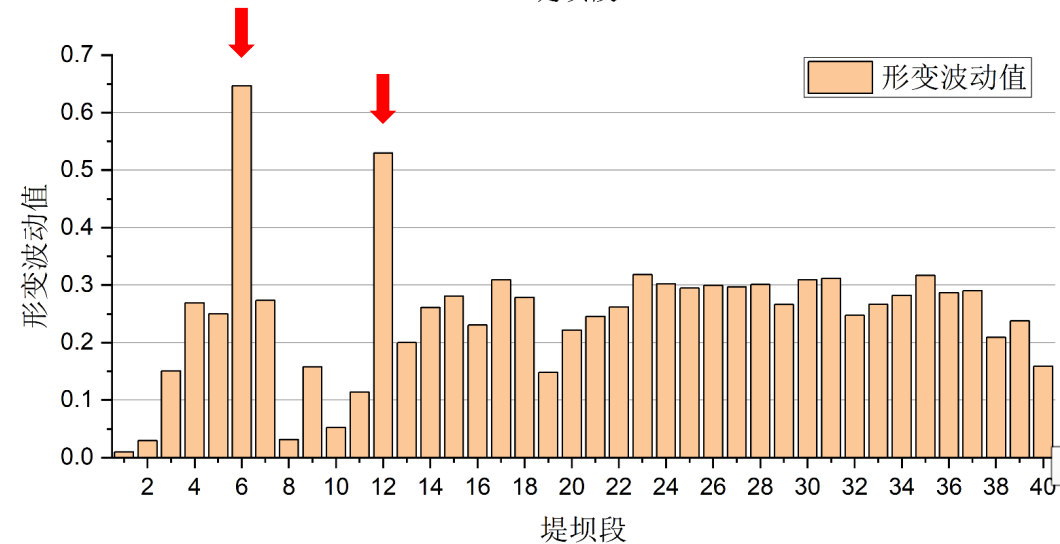
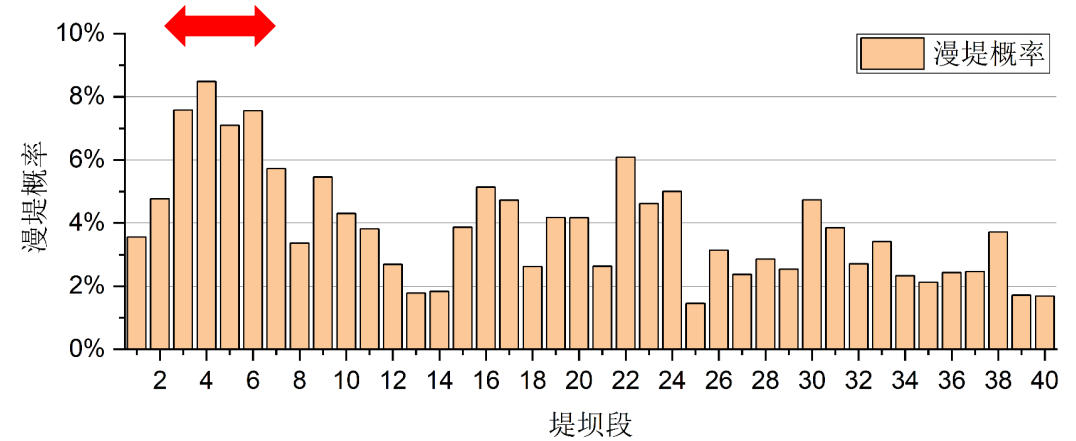
➤ The Deformation-based Probability of Seawall Failure

Probability of overtopping

- Segments 3-6 have higher probability ($>7\%$)
- Segments 13, 14, 25, 39, and 40 have lower probability ($<2\%$)
- There is a nonlinear negative correlation between the corrected seawall-height and the probability of overtopping

Probability of levee-breach

- Segments 6 and 12 have higher probability
- Segments 1, 2, 8, and 10 have lower probability
- The levee-breach indexes of eastern seawalls (segments 16-40) are similar.





Flood Hazard

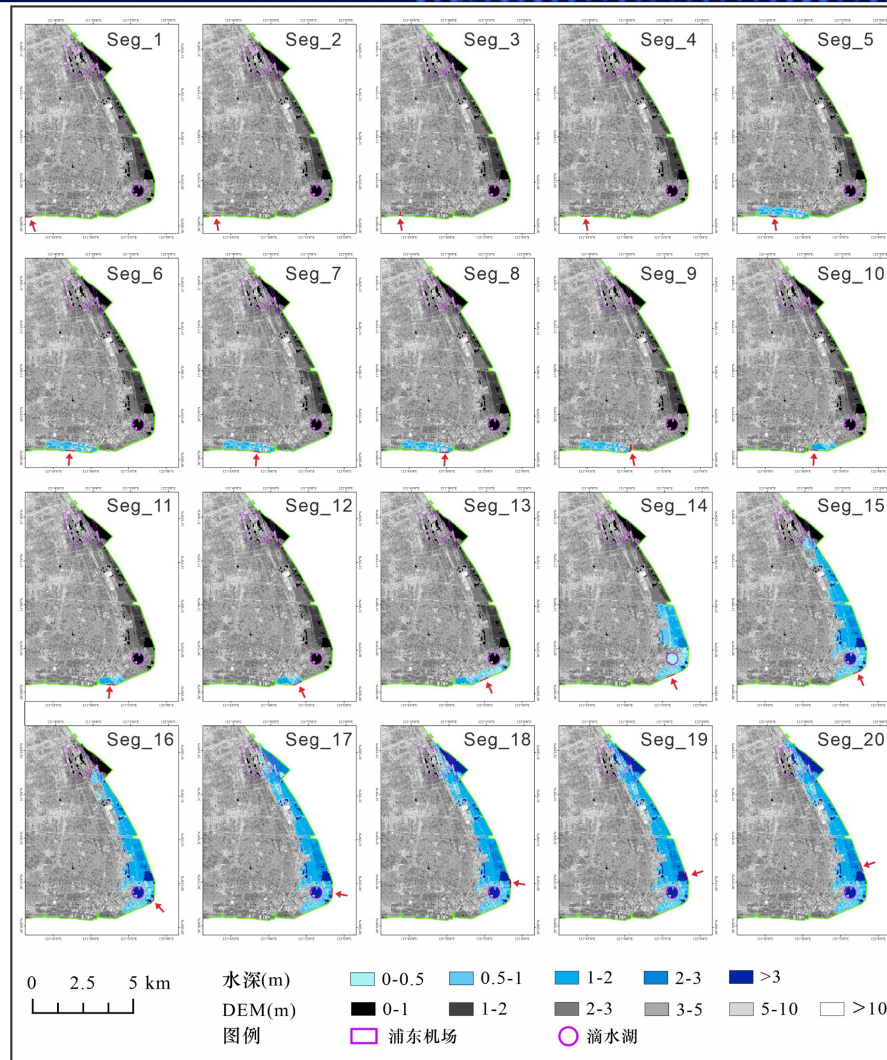
Segments 1-4 and 39-40



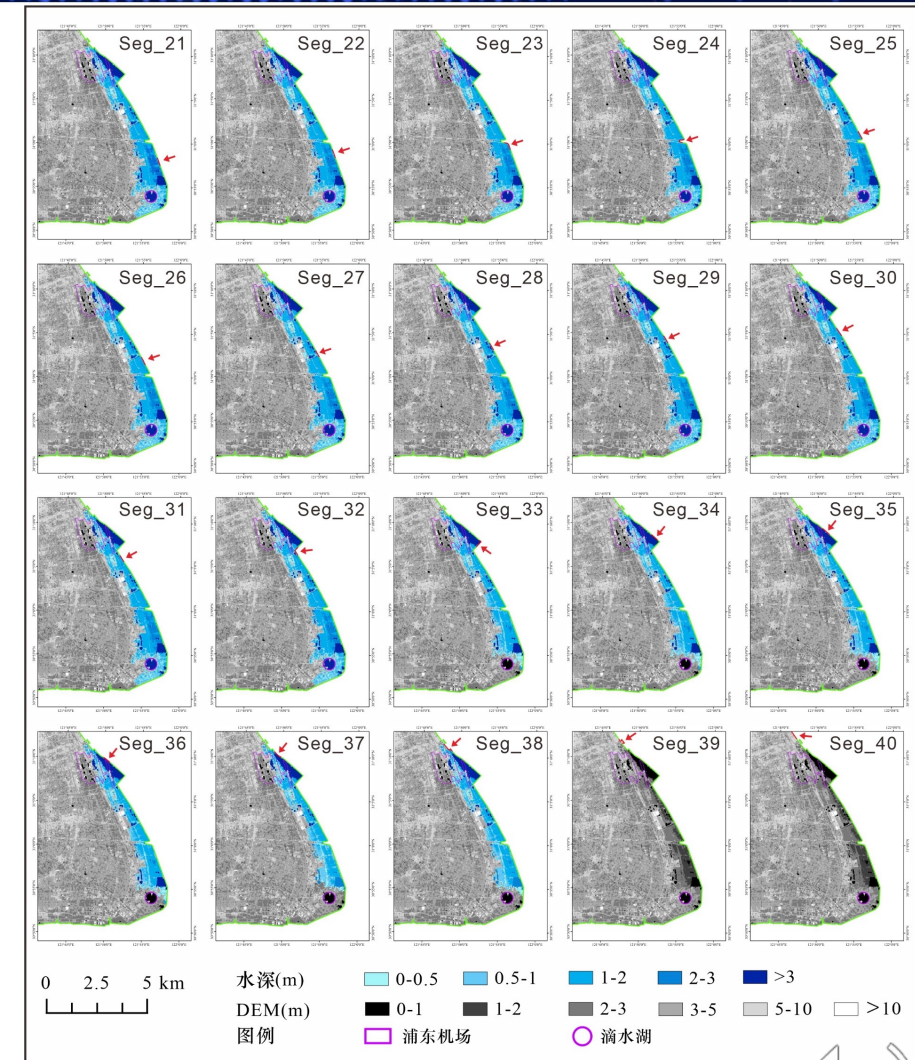
Segments 5-14



Segments 15-38



Simulated inundation scenarios 1-20 for a 100-year return period flood in Shanghai.



Simulated inundation scenarios 21-40 for a 100-year return period flood in Shanghai.



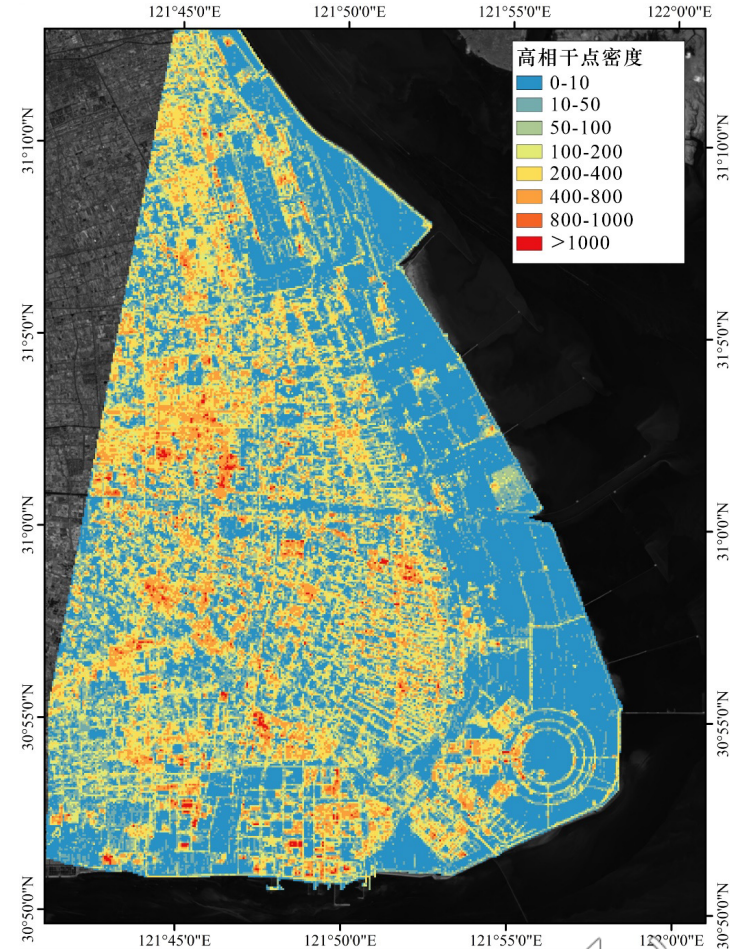


➤ Vulnerability

- The high-coherent points, that are coherent at both low and up Doppler bands, were extracted
- The high-coherent points are mainly distributed in artificial building areas.



The distribution map of high-coherent points superimposed on Sentinel-2 true color image of Shanghai.

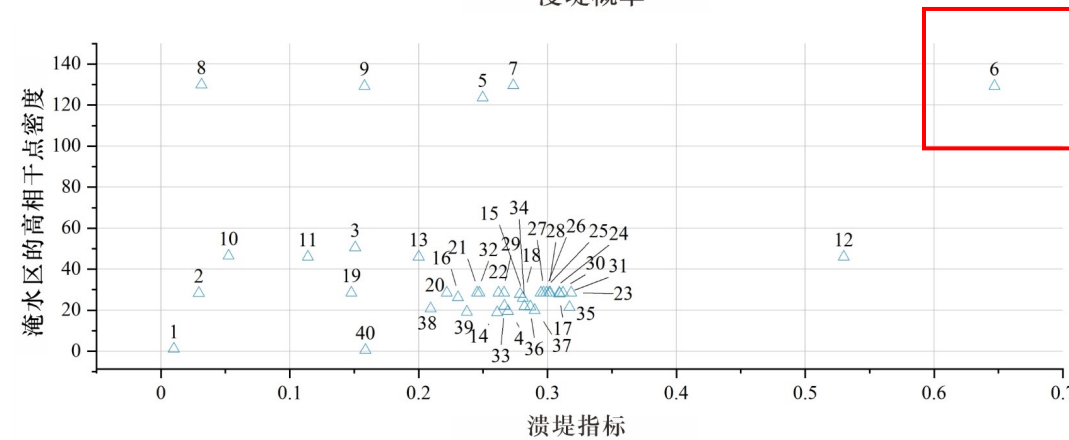
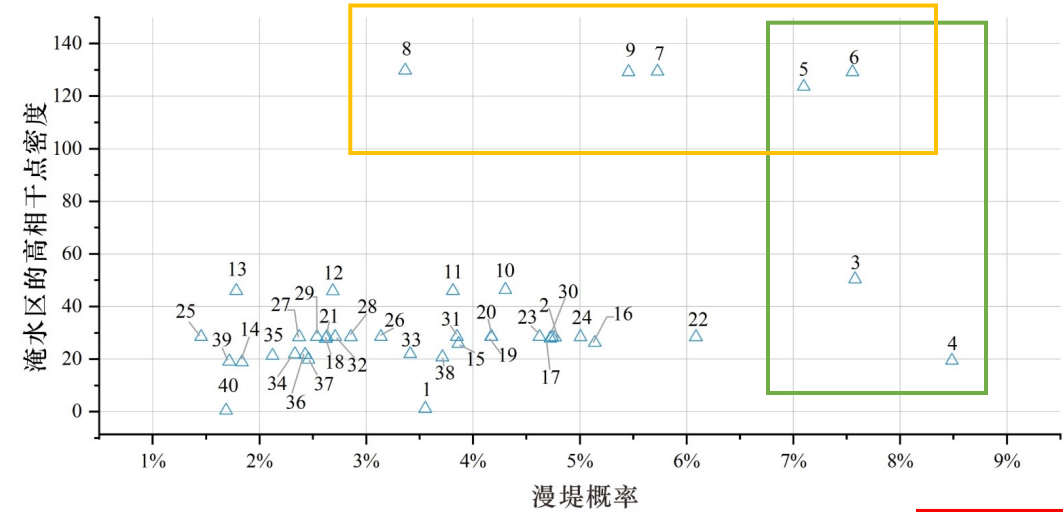


The density map of high-coherent points in Shanghai.



➤ Risk Assessment of Seawall Failure

- The X-axis shows the failure probability, and Y-axis is the impact of a flood, measured as the density of high-coherent points in the flooded areas.
- Segments 3-6 have higher probability of overtopping (>7%). And for segments 5-9, the density of high-coherent points is high.
- Levee-breach index and density of high-coherent points within inundation areas for segment 6 is high.



Map of Failure probability-Density of high-coherent points within inundation areas for 40 segments in Shanghai.



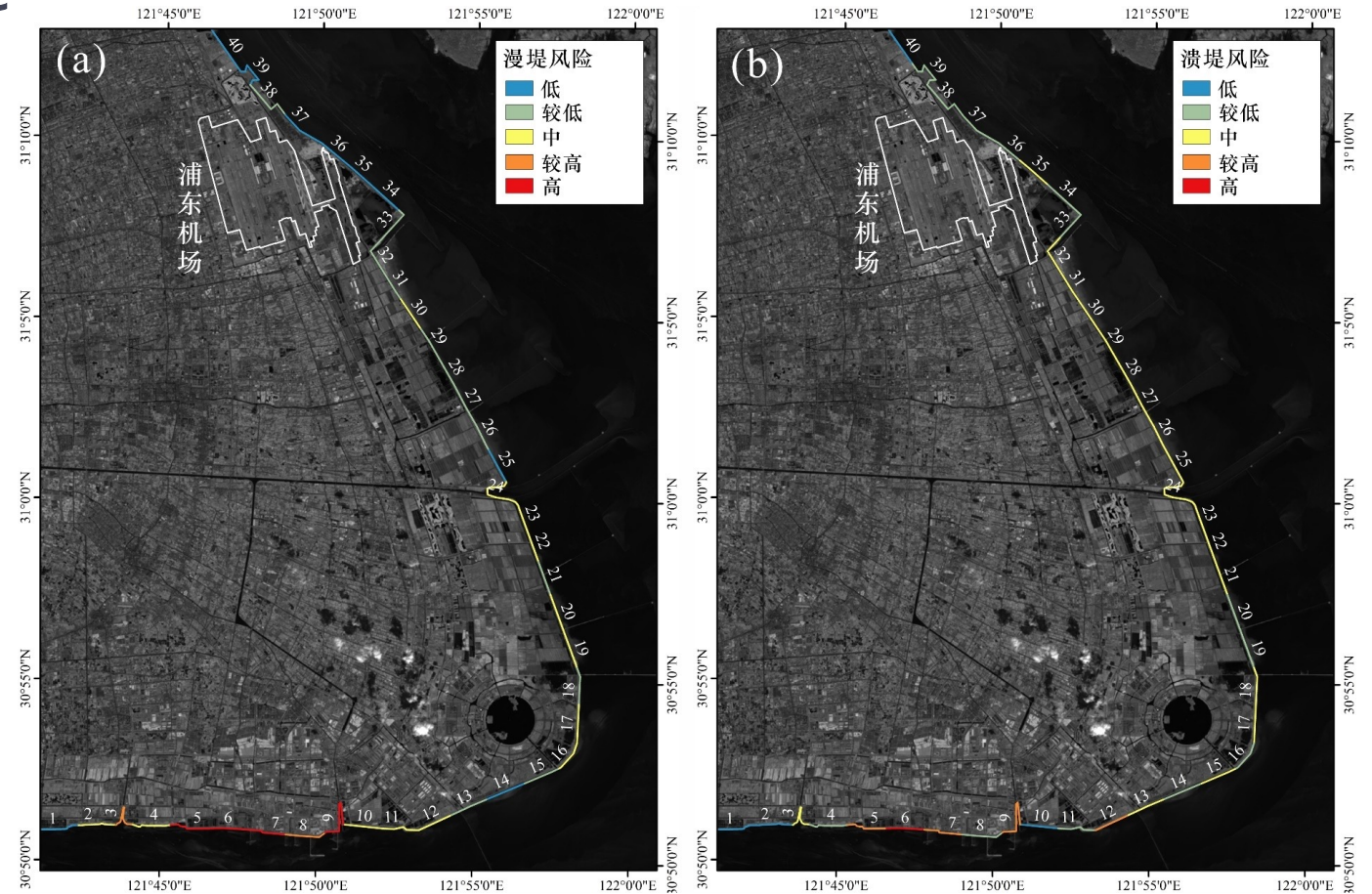


➤ Risk Assessment of Seawall Failure

- The risks of seawall failure have five levels: high, medium-high, medium, medium-low and low.
- Segments 5, 6, 7, 9 have higher probability of overtopping.
- Only segment 6 has high-level risk of levee-breach.



Segment 6 is the 'key segment'







Maps of overtopping (a) and levee-breach (b) risks for 40 segments in Shanghai.



Article

Change Detection Techniques with Synthetic Aperture Radar Images: Experiments with Random Forests and Sentinel-1 Observations

Pietro Mastro ¹, Guido Masiello ¹, Carmine Serio ¹ and Antonio Pepe ^{2,*}

¹ School of Engineering, University of Basilicata, 85100 Potenza, Italy; pietro.mastro@unibas.it (P.M.); guido.masiello@unibas.it (G.M.); carmine.serio@unibas.it (C.S.)

² Institute for Electromagnetic Sensing of the Environment (IREA), Italian National Research Council, 328, Diocleziano, 80124 Napoli, Italy

* Correspondence: pepe.a@irea.cnr.it; Tel.: +39-0817620617



Change Detection Techniques with Synthetic Aperture Radar Images: Experiments with Random Forests and Sentinel-1 Observations

This paper addressed a review of the theory of existing coherent and incoherent CD methodologies for disaster management (i.e., wildfires or floods) using SAR images.

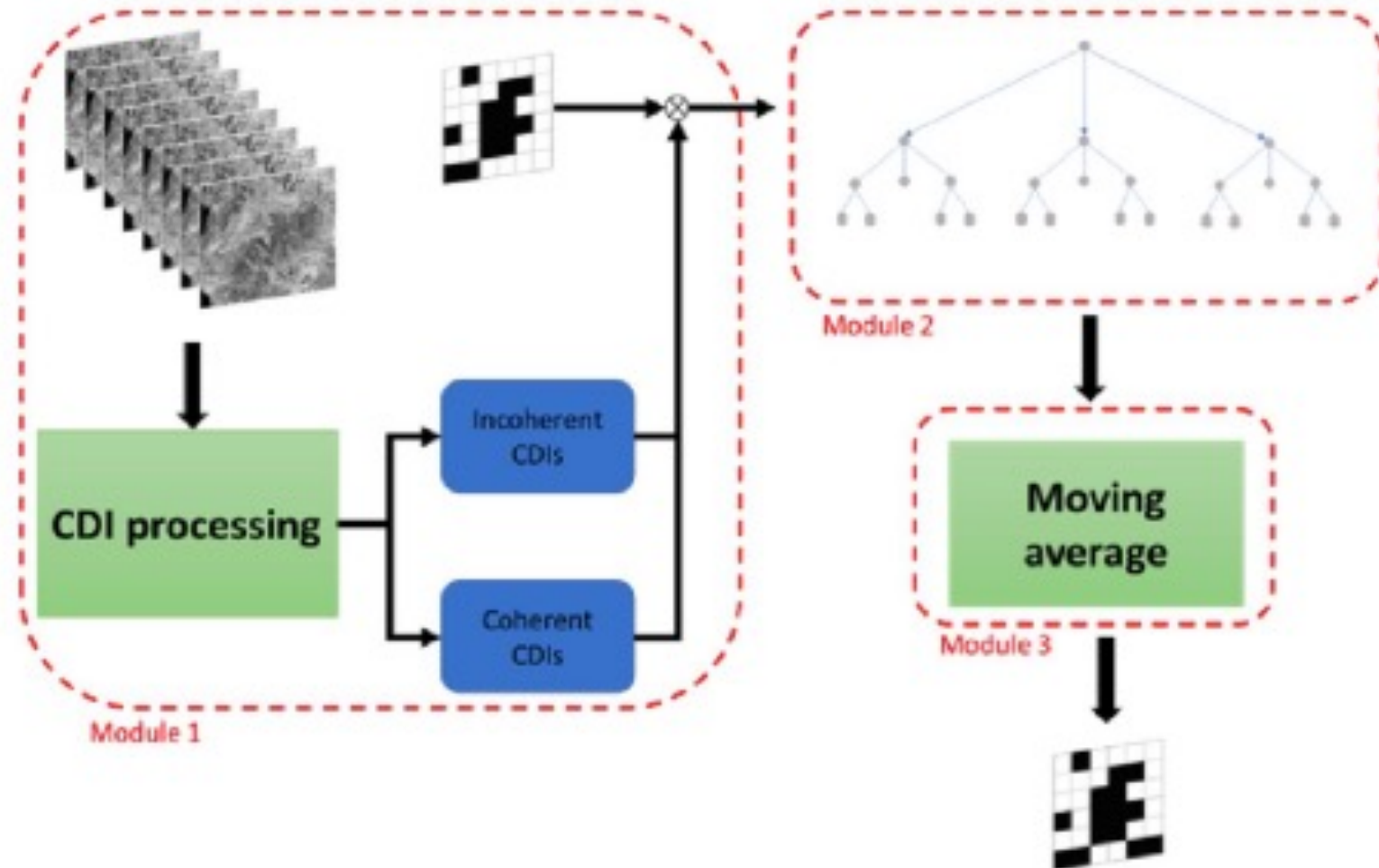
We focused on new trends of evolution on Change Detection with SAR data, by addressing the emerging ML-driven CD approaches.

We investigated the potential of different synthetic coherent/incoherent CDIs and their mutual interactions for the rapid mapping of “changed areas.”

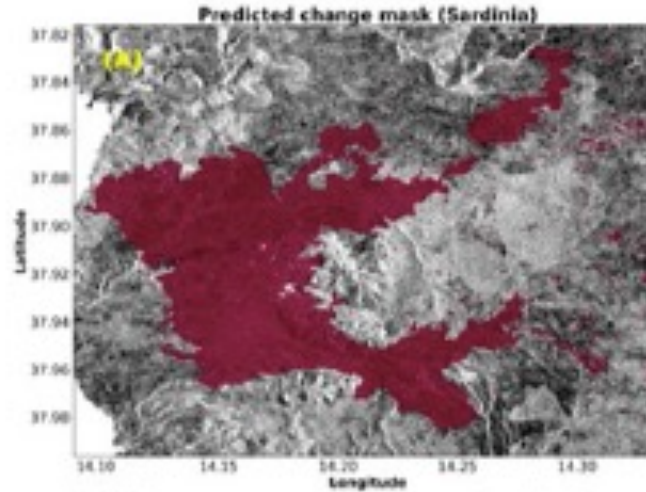
A classifier based on RF was trained combining different information from coherent/incoherent CDIs over different AOIs characterized by wildfire and flood phenomena.



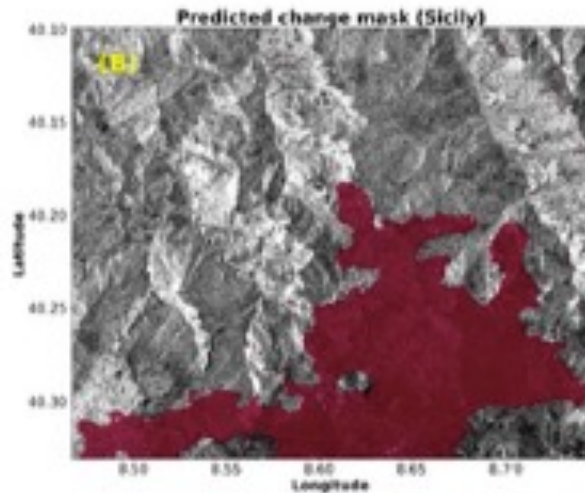
Change Detection Techniques with Synthetic Aperture Radar Images: Experiments with Random Forests and Sentinel-1 Observations



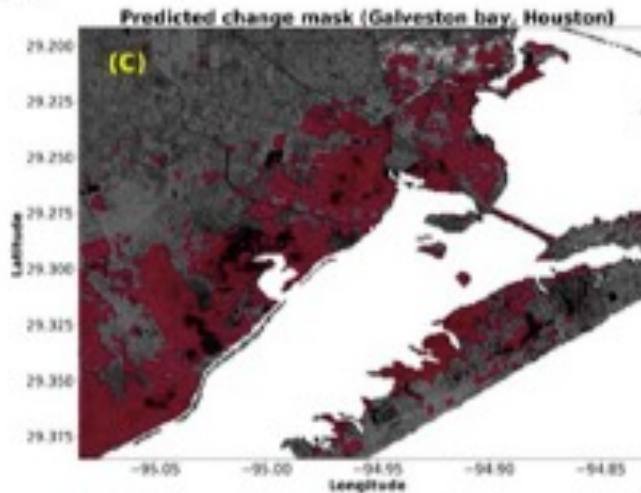
Change Detection Techniques with Synthetic Aperture Radar Images: Experiments with Random Forests and Sentinel-1 Observations



Sardinia Fire



Sicily Fire



Galvestone, Flood



IEEE TRANSACTIONS ON GEOSCIENCE AND REMOTE SENSING

Phase Closure Inconsistencies of Multi-look SAR Interferogram Triplets

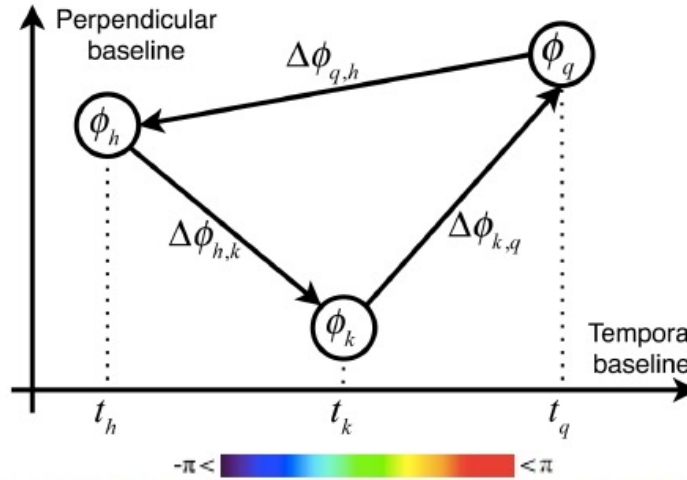
Francesco Falabella, *Graduate Student Member, IEEE*, and Antonio Pepe, *Senior Member, IEEE*





- The measure of the Earth's ground deformation using Mt-InSAR) algorithms represents a consolidated practice.
- Among the different Mt-InSAR processors, a significant role is played by those algorithms based on small-baseline (SB) multi-look (ML) interferograms.
- The multi-look operation involves the average of the information relating to each family of scatterers in the single look (SLC) pixels.
- Recently, it has been observed that some inconsistencies in the InSAR products (i.e., ground deformation time-series and mean deformation velocity maps) may happen when sets of multi-look SAR interferograms with very short temporal baselines are processed.
- Such spurious signals lead to systematic biases that might lead to unreliable InSAR ground displacement products

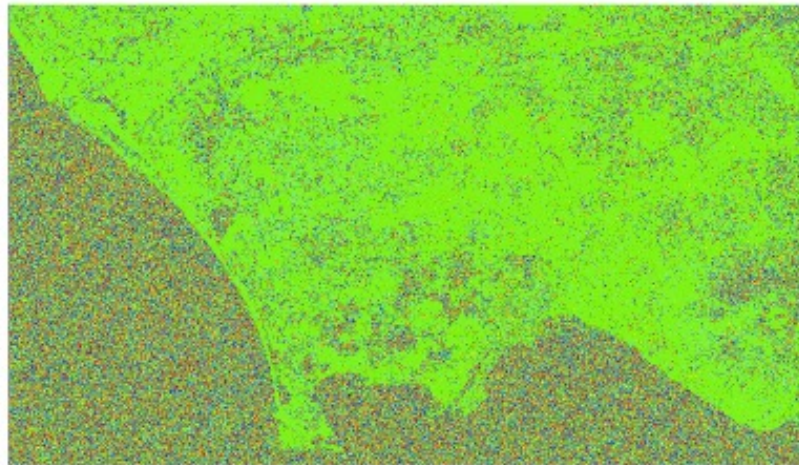




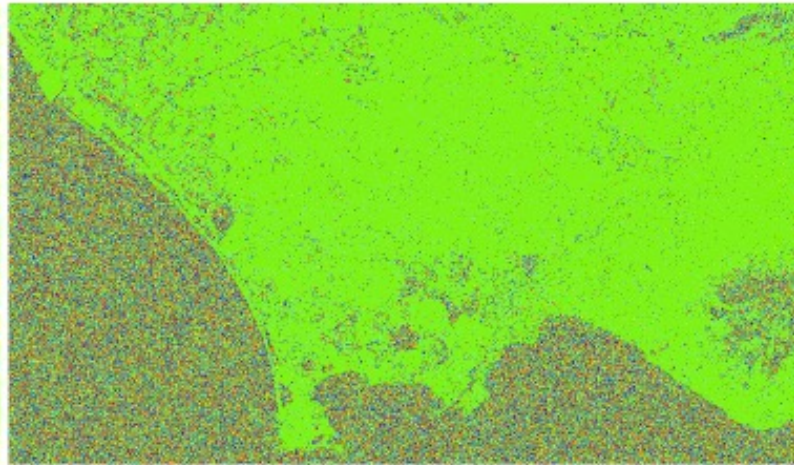
$-\pi < \text{color scale} < \pi$

$-\pi < \text{color scale} < \pi$

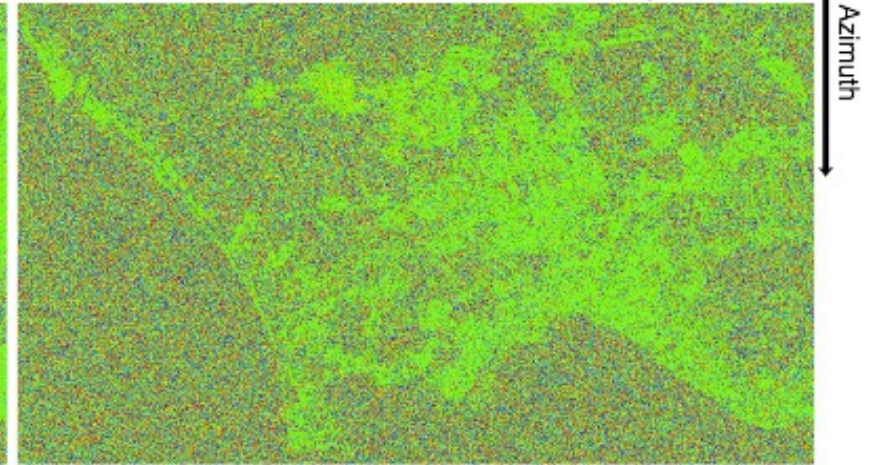
$-\pi < \text{color scale} < \pi$



(a)



(b)



(c)

Fig. 6. COSMO-SkyMed phase triplets over the Gulf of Naples, Italy. a) Triplet's epochs: 2011-06-17, 2011-06-18, and 2011-06-21. Triplet's average absolute perpendicular baseline: 140 m. b) Triplet's time instants: 2010-02-14, 2010-02-22, and 2010-02-23. Triplet's average absolute perpendicular baseline: 138 m. c) Triplet's time instants: 2010-07-24, 2010-08-25, and 2010-10-12. Triplet's average absolute perpendicular baseline: 246 m.

Let us assume that the biased phases are time-invariant, i.e., the bias phenomena depends only on the temporal baseline values $\Delta t_{h,k}$, thus we model the InSAR biased phases with a second order expansion as follows:

$$\Delta\phi_{h,k}^{bias}(\Delta t_{h,k}) \cong [v + \Delta v(\Delta t_{h,k})] \Delta t_{h,k} \quad (1)$$

where v is a constant decay phase velocity factor and Δv is a temporal-baseline-dependent phase velocity difference term. If we consider two generic interferometric SAR data pairs with temporal baselines $(\lambda - 1)\delta$ and $\lambda\delta$, where δ is the repetition time of the considered SAR constellation (i.e., 6 days for Sentinel-1A/B sensors) and , Equation (1) particularizes as:

$$\Delta\phi^{bias}(\lambda\delta) \cong [v + \Delta v(\lambda\delta)] \lambda\delta \quad (2)$$

$$\Delta\phi^{bias}[(\lambda - 1)\delta] \cong \{v + \Delta v[(\lambda - 1)\delta]\} (\lambda - 1)\delta \quad (3)$$

Equations (2) and (3) can properly be combined with each other, and the following iterative relation is found:

$$\Delta\phi^{bias}[(\lambda - 1)\delta] \cong \frac{\lambda - 1}{\lambda} \Delta\phi^{bias}(\lambda\delta) + \{\Delta v[(\lambda - 1)\delta] - \Delta v(\lambda\delta)\} (\lambda - 1)\delta \quad (4)$$



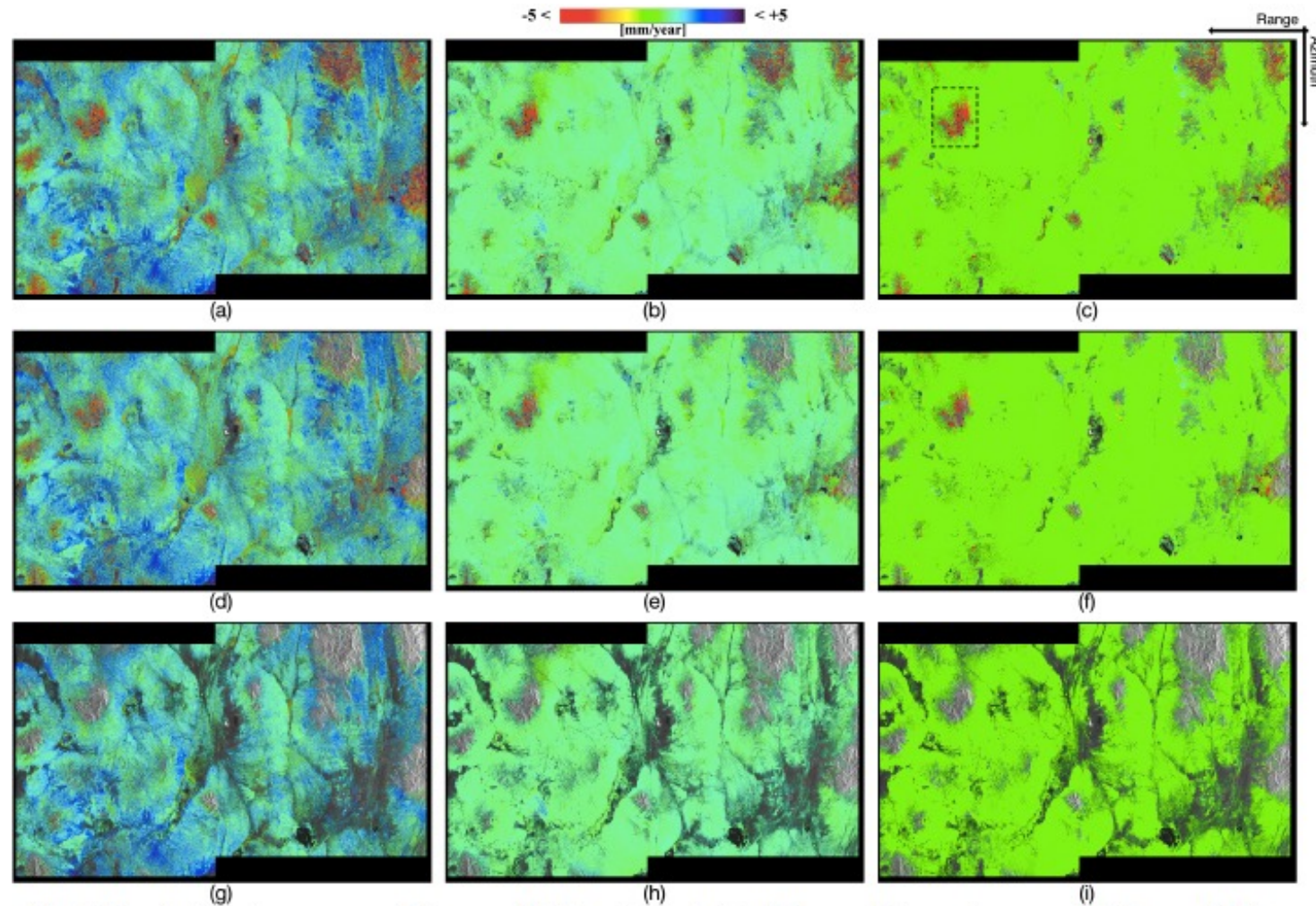
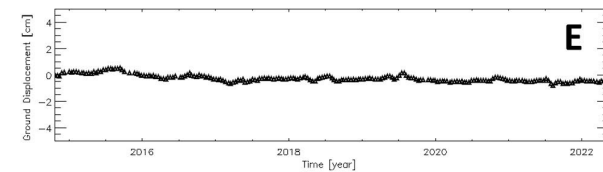
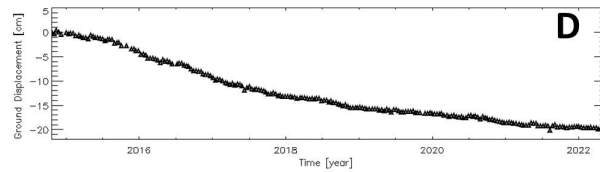
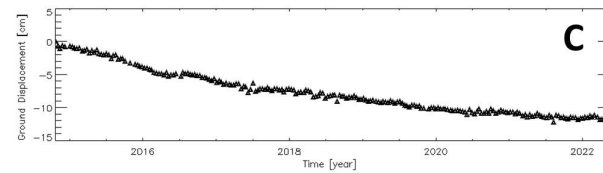
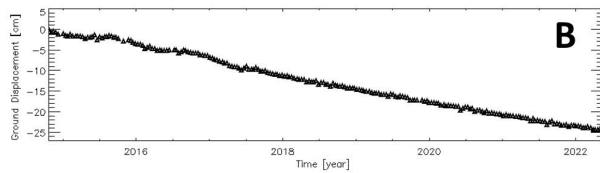
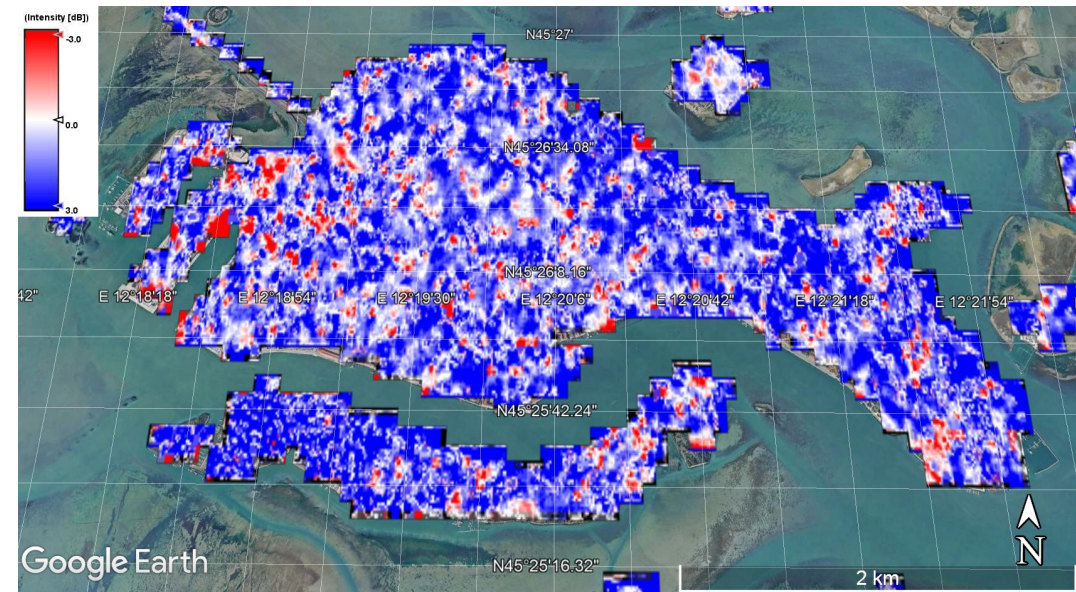
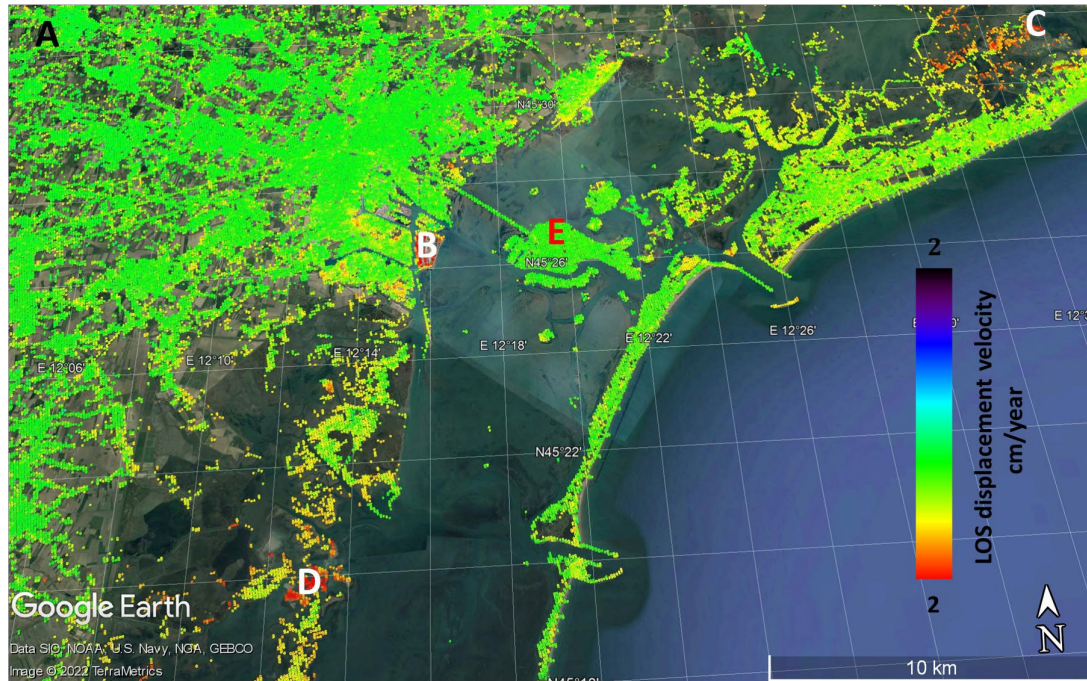


Fig. 1. Nevada test-site area maps of the ground deformation velocity differences between the case at 12 days and 96 days, where only pixels larger than given values of the temporal coherence are depicted. a), d) and g) Ground deformation velocity bias considering the original interferograms. b), e) and h) Ground deformation velocity bias when the time-invariant correction method is applied. c), f) and i) Ground deformation velocity bias when the time-variant correction method is applied. a)-c) Temporal coherence ≥ 0.7 . d)-f) Temporal coherence ≥ 0.9 . g)-i) Temporal coherence ≥ 0.98 .





Other Activities



$$LR_{VH} = \ln(\langle X_{post}^{VH} \rangle) - \ln(\langle X_{pre}^{VH} \rangle) \quad (1)$$

$$LR_{VY} = \ln(\langle X_{post}^{VY} \rangle) - \ln(\langle X_{pre}^{VY} \rangle) \quad (2)$$

$$LR_{VH_YV} = LR_{VH} + LR_{VY} \quad (3)$$





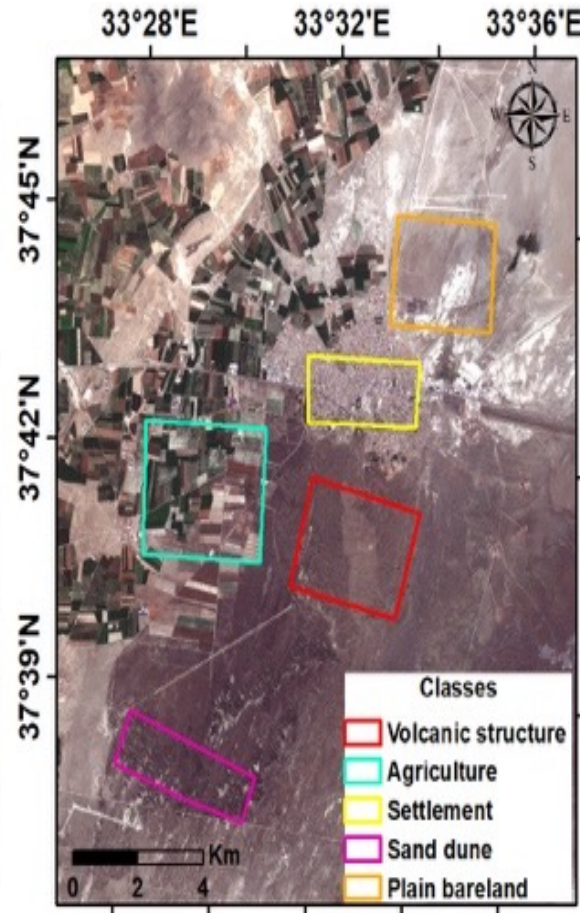
Other Activities from the Turkish Group of Hacettepe University, Ankara and Technical University of Istanbul

- We explore a new DEM derived from the repeat-pass InSAR method over a semi-arid region where karstic and volcanic structures are present;
- We explore first time the multi-temporal InSAR results of X-band PAZ data for DEM extraction
- Additionally, multi-temporal small scale displacements are also derived using repeat-pass interferograms



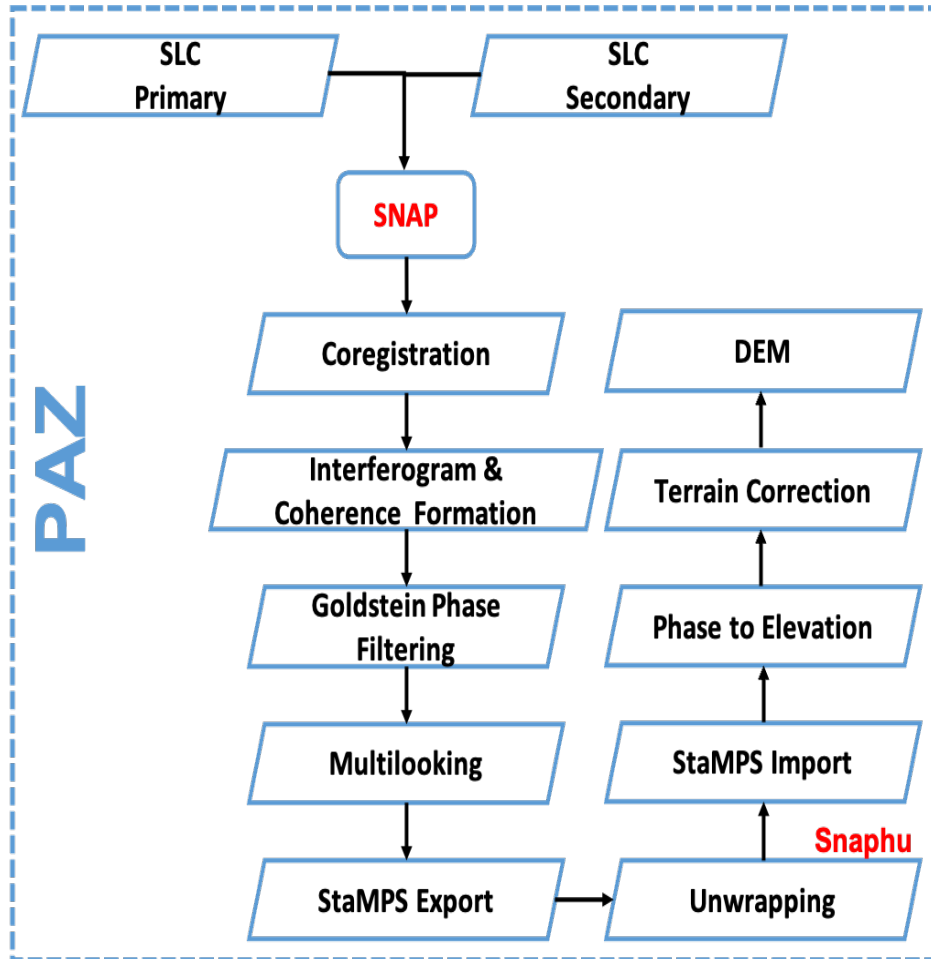


Other Activities



- Konya closed basin is located in the center of the Anatolia region.
- The study case has different geological, archaeological, and cultural areas
- Widespread young volcanic formations
- Climate condition is mostly semi-arid
- Five regions were considered



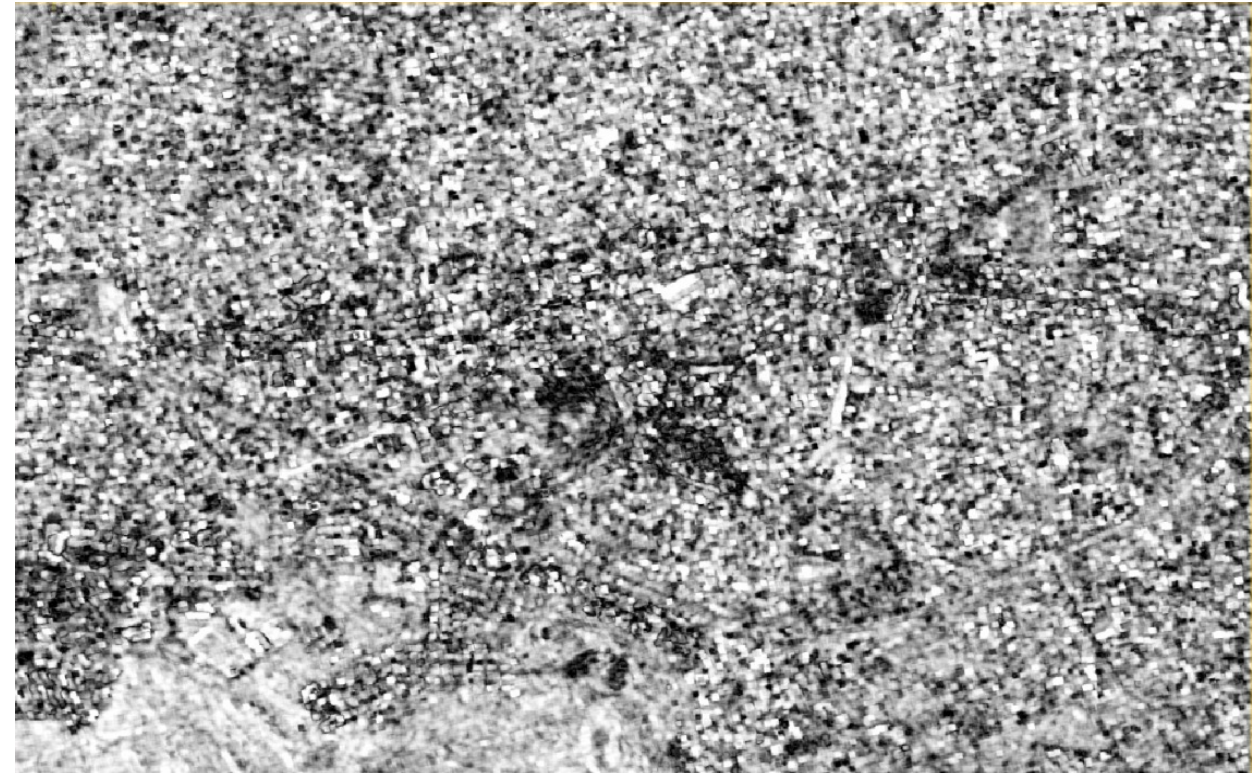


- Open-Source Sentinel Application Platform (SNAP) software
- The coherence information indicates the cross-correlation coefficient between two co-registered complex data and the quality of the product

$$\gamma = \frac{|\langle S_1 S_2^* \rangle|}{\sqrt{\langle S_1 S_1^* \rangle \langle S_2 S_2^* \rangle}}$$

where S_1 and S_2 = complex matrices of backscatter coefficient of the SAR image pair
 * = complex conjugation
 $\langle \rangle$ = indicates spatial averaging





RGB:19 Nov-30 Nov-30 Nov (Pair1)

- TanDEM-X showed min RMSE compared to PAZ results.
- The RMSE values range between 0.88 m on bareland and 2.4 m on settlement.
- The lowest RMSE of TanDEM-X is detected on bareland (0.87m) which gave the lowest RMSE with PAZ data (2.36m)

